

Learning Energy Based Inpainting for Optical Flow^{*}

Christoph Vogel¹[0000-0002-5960-1375], Patrick Knöbelreiter¹[0000-0002-2371-014X], and Thomas Pock^{1,2}[0000-0001-6120-1058]

¹ Graz University of Technology, Graz, Austria.
 {firstname.lastname}@icg.tugraz.at

² Austrian Institute of Technology, Vienna, Austria

Abstract. Modern optical flow methods are often composed of a cascade of many independent steps or formulated as a black box neural network that is hard to interpret and analyze. In this work we seek for a plain, interpretable, but learnable solution. We propose a novel inpainting based algorithm that approaches the problem in three steps: feature selection and matching, selection of supporting points and energy based inpainting. To facilitate the inference we propose an *optimization layer* that allows to backpropagate through 10K iterations of a first-order method without any numerical or memory problems. Compared to recent state-of-the-art networks, our modular CNN is very lightweight and competitive with other, more involved, inpainting based methods.

Keywords: Optical Flow · Energy Optimization · Deep Learning.

1 Introduction & Related Work

The computation of optical flow, the apparent 2D motion field between two consecutive frames of a temporal image sequence, is one of the most investigated problems in computer vision. Optical flow possesses a vast number of applications, among others, video processing for action detection or activity recognition, autonomous driving [22] or medical imaging. Similarly, there are multiple methods, to compute the optical flow field. Energy based techniques that were popular in the past, are now outperformed and replaced by approaches that solely rely on convolutional neural networks (CNNs) [11,21]. Despite their great performance on benchmark data sets, these networks often lack interpretability – often it remains unclear, apart from input and loss function, how the network internally models the flow problem. In this work we seek to combine both ideas. We propose to utilize an energy based optimization problem suitable for the computation of optical flow and let the network learn the input to the energy. We then minimize the energy to produce the flow field by unrolling the iterations of a first-order algorithm. Our energy is convex but non-smooth and hence demands for a large number of iterations. To address the memory and numerical problems that occur when running backpropagation for more than 10K iterations on the GPU,

^{*} Supported by the ERC starting grant 640156, HOMOVIS

we propose an *optimization layer*, that handles these problem in an efficient GPU implementation using *checkpointing* [14,8] and buffering of intermediate solutions in double precision. Our energy minimizing network layer is related to ideas proposed in [3]. Compared to [3], we solve a non-linear and non-smooth problem, but similarly facilitate to backpropagate through the minimization process. However, our experiments indicate that the increased robustness provided by the non-smooth formulation is beneficial for our optical flow problem. A combination of CNNs and energy optimization was also proposed by [40,30,35]. Here, we seek to run our optimization until near convergence. Our optimization layer allows us to unroll 4 orders of magnitude more iterations than [40,30].

For our model we consider a class of algorithms that treat the computation of optical flow as a form of *inpainting* or sparse-to-dense interpolation problem. Possibly the most prominent representative of these methods is [28] that tackles the problem in many different steps, including sparse matching [37], edge detection [10], computing super-pixels [1], variational refinement [6], and various post-processing steps. Here, we simplify the inpainting process to its core, feature generation to build a cost volume for image matching, selection of supporting matches and inpainting via energy minimization. We tackle the problem via deep learning and propose a network structure that still delivers interpretable intermediate results, and allows for training in end-to-end fashion. In contrast to other inpainting based optical flow methods, we start our process from dense matching. Consequently, we are not committed to a pre-selection of, possibly incomplete or unmatchable interest points [37,41], but can select the supporting pixels *after* matching. Compared to nearest neighbor field methods [18,36], we make use of a complete cost-volume and avoid a coarse-to-fine scheme or hashing. To that end, we make use of a recent result [23] that allows for a low memory footprint of the cost volume. In contrast to network based solutions to inpainting [41], we maintain the interpretability of an energy based framework.

The core idea of our algorithm is closely related to diffusion based inpainting for image compression [12]. Here, the compression ratio is mainly dependent on the selection of *supporting points* from which the image is then inpainted. Given the image to be compressed, this selection process can be formulated as a bi-level optimization problem [9,25]. Unfortunately, we have no knowledge of the ground-truth reconstruction and have to select the supporting points from a large number of possible matches per pixel. Here, our method estimates the confidence of the different matches per pixel. In the context of stereo matching confidence estimation is a well studied problem [16]. Lately also CNN based solutions have been proposed [2,26]. Compared to the general problem, our solution is directly task related. We are not interested in providing a confidence for each pixel, but also have to consider the relevance of a pixel to our inpainting task. Our selection process has to balance the added information content and robustness of the match on a per pixel basis. This is addressed by learning confidence estimation and inpainting in end-to-end fashion.

In this paper, we propose a novel, 'from scratch' algorithm for inpainting optical flow. We reduce the process to its core: feature computation and matching,

selection of supporting pixels and energy based inpainting. Compared to recent state-of-the-art networks, our CNN is lightweight with only 450K parameters. We introduce a novel *quad-fitting* layer that can learn features for sub-pixel accurate matching, while still allowing for large displacements and finally propose an *optimization layer* to solve the energy minimization problem. Here, we show that a tailored GPU implementation can lead to memory and numerical efficiency and facilitate backpropagation over more than 10K iterations.

2 Method

In this work we consider the estimation of optical flow, the 2D motion field that describes the movement of pixels between two consecutive frames $I^0, I^1 \in \Omega \subset \mathbb{R}^2$ of an image sequence defined over the domain Ω . Formally, we define the optical flow field as $\mathbf{u} := (u_0, u_1)^\top$, consisting of a vertical and a horizontal component given by the functional $u_i : \Omega \rightarrow \mathbb{R}, i \in \{0, 1\}$. Here, we let super-indices encode the time step and sub-indices the motion direction. We formulate the task of estimating such motion field as a classical inpainting/denoising problem:

$$\min_{u_i} \mathcal{R}_1(u_i) + \int_{\Omega} c(x)|u_i(x) - \hat{u}_i(x)|dx, \quad \text{with } \mathcal{R}_1(u_i) := \int_{\Omega} |W^{\frac{1}{2}}\nabla u_i|_{\delta} dx, \quad (1)$$

which corresponds to weighted Total Variation [31] regularization with a robust weighted ℓ_1 data fidelity term, known to lead to piecewise constant solutions. Here, $|\cdot|_{\delta}$ denotes the Huber-norm $|\cdot|_{\delta} := \frac{1}{2}|\cdot|_2^2 + \frac{1}{2}\delta^2$, if $|\cdot|_2 \leq \delta$ and $\delta|\cdot|_2$ else. Likewise, we also consider a variant corresponding to weighted Total Generalized Variation [5] of second order, where we replace the regularization term by:

$$\mathcal{R}_2(u_i) = \min_{w_i=(w_{i,0}, w_{i,1})^\top} \int_{\Omega} |W^{\frac{1}{2}}\nabla u_i - w_i|_{\delta} + \beta(|\nabla w_{i,0}|_{\delta} + |\nabla w_{i,1}|_{\delta})dx, \quad (2)$$

where $w_{i,j} \in \Omega \rightarrow \mathbb{R}, i, j \in \{0, 1\}$ represent auxiliary variables. In contrast to (1), (2) prefers a piecewise affine solution for the flow components u_i . Both cases require a good guess for the initial flow $\hat{\mathbf{u}} := (\hat{u}_0, \hat{u}_1)^\top$, the *diffusion tensor* $W := \text{diag}(\omega_0, \omega_1)$, c.f. [38] and the *confidence score* $c \in [0, 1]$ that locally ties the solution \mathbf{u} to the initial estimate $\hat{\mathbf{u}}$. To compute \mathbf{u} we use a CNN that is split into different parts to deliver the inputs for our optimization stage solving (1) or (2). In particular, we perform dense pixel-wise matching using network generated features, refine the matches by locally fitting a quadratic to the cost and employ the arg min cost solution as initial estimate. Diffusion Tensor W and confidence c are provided by 2 sub-networks. All these CNNs are rather small, with around 150k parameters each. To solve our optimization problem we employ a special custom layer that allows to accurately minimize convex, non-smooth problems in the form of (1) or (2) and provides a simple, memory efficient and accurate way to backpropagate through them and, thus, learn its input parameters.

An overview of our method and the progression of our framework is provided in Fig. 1. The input images pass the feature extraction stage from which the

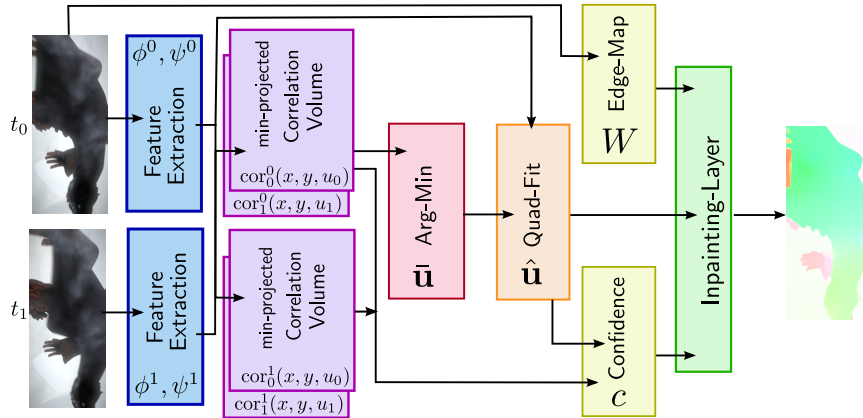


Fig. 1. The overview of our pipeline. Feature vectors are generated from the input images. Per view, in forward and backward direction, two (see Sec. 2.1) correlation volumes are built. A preliminary solution $\hat{\mathbf{u}}$ is obtained by refining the flow at minimal (negative) correlation $\bar{\mathbf{u}}$ in the *quad-fitting layer* (see Sec. 2.2). Afterwards, a confidence c is computed for each flow vector obtained from the fitting. In parallel, a diffusion tensor or edge-map W is generated (Sec. 2.3). Confidence, tensor and preliminary solution $\hat{\mathbf{u}}$ are fed into our optimization layer (Sec. 2.5) that solves problem (1) or (2).

cost volumes are constructed. We employ the method of [23] and generate 2 3D volumes from one complete 4D cost volume (c.f. Sec. 2.1). This allows to train the feature generation step on whole images instead of small patches and also enables us to compute cost volumes in forward and backward direction, which are later used for our confidence estimates. To keep the network simple and small we do not consider filtering of the cost volumes, e.g. [32,15,29]. Instead, we directly use the solution with maximal correlation for both forward ($\bar{\mathbf{u}}$) and backward direction ($\bar{\mathbf{u}}^{\text{BW}}$). Our *quad-fitting layer* (Sec. 2.2) delivers sub-pixel accurate matches, by fitting a quadratic function to the local feature cost. The computed pixel-wise estimates $\hat{\mathbf{u}}$, along with some extra features like the softmax-probabilities are fed into a network to compute the confidence scores c , c.f. Sec. 2.4. Further, we generate the diffusion tensor, or edge-map, W applying a network that receives the images as input, described in Sec. 2.3. The initial estimates $\hat{\mathbf{u}}$ the confidence scores c and the diffusion tensor W are the fed into our optimization layer to compute the final solution (Sec. 2.5).

Following the flow of our pipeline, we now consider each of its stages in detail.

2.1 Feature Generation

For feature generation we follow [23] and employ a Siamese network consisting of two convolutional branches with shared parameters. In our implementation we utilize a feed forward network comprised of 5 convolutional layers with a filter size of 3×3 and 64 channels, followed by a single 1-D convolution. After each

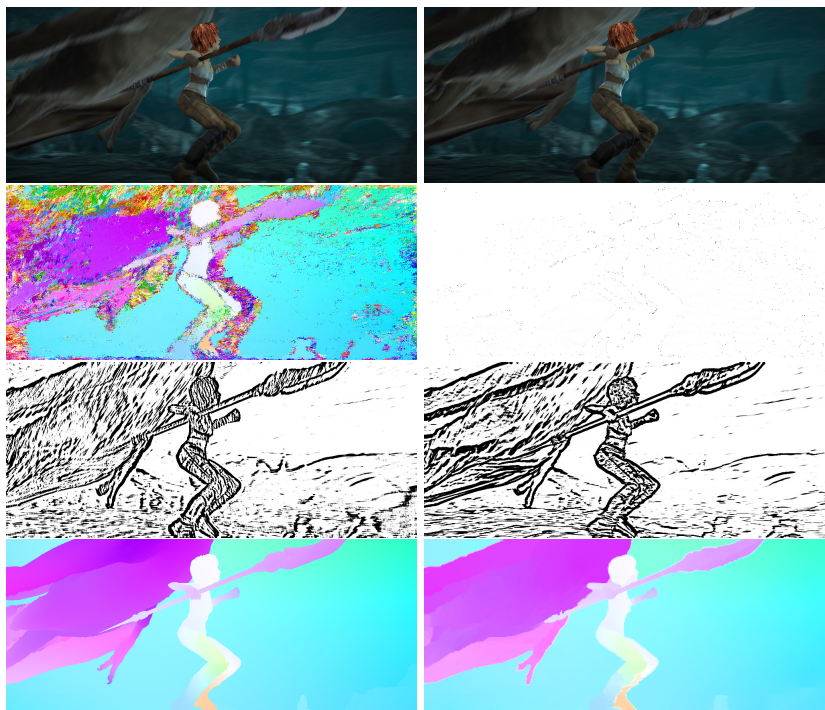


Fig. 2. *Top:* Input images at time step 0 (left) and time step 1 (right). *Second row:* Data term \hat{u} (left) and confidence map c (right), where black means high and white low confidence. *Third row:* Diffusion tensor W . Horizontal edges, W_0 (left) and vertical edges, W_1 (right). Here white means strong and black weak regularization. *Bottom:* The ground truth solution (left) and the output of the optimization layer.

stage we apply a tanh non-linearity. Further, we utilize dilated filters [39] of sizes 1, 2, 4, 1, 4 and 1 in the stages. In the fourth layer we apply a striding of 2 and reduce the feature maps by a factor of 2 in each dimension of our domain Ω . We retain the feature maps (ψ^0 and ψ^1) after the third layer for our sub-pixel refinement step described in Sec. 2.2. The final feature maps ϕ^0 and ϕ^1 of the two frames are fed into a correlation layer that generates four 3D cost volumes:

$$\text{cor}_i^j(x, y, u_i) := \min_{u_{1-i} \in H} -\langle \phi^j(x, y), \phi^{1-j}(x + u_0, y + u_1) \rangle, \quad i, j \in \{0, 1\}. \quad (3)$$

$H := \{-d, \dots, d-1\}$ denotes our range of integer displacements, which effectively correspond to a twice as large displacement at the original resolution due to the striding. Note that we explicitly consider the forward (cor_i^0) and backward direction (cor_i^1) and split the full 4D cost volumes $\text{cor}^j(x, y, u_0, u_1)$ into two directional ones, c.f. (3). To that end, [23] proposes to use *min-projection* to eliminate one of the motion directions via: $\text{cor}_i^j(x, y, u_i) := \min_{u_{1-i} \in H} \text{cor}^j(x, y, u_0, u_1)$. Most prominently this reduces the memory complexity of storing the cost volume from

quadratic to linear. Our initial discrete motion estimates can then be found as $\bar{u}_i := \arg \min \text{cor}_i^0(x, y, u_i), i = 0, 1$. Note, that the arg min remains untouched by the *min-projection* operation applied beforehand on the cost volumes. Further, we can define a probability for each pixel and possible displacement via the usual *softmax* function for the reference view 0:

$$p_i(x, y, u_i) := \exp(-\text{cor}_i^0(x, y, u_i)) / \sum_{u_i \in H} \exp(-\text{cor}_i^0(x, y, u_i)), \text{ for } i = 0, 1. \quad (4)$$

Those (pseudo-)likelihoods, evaluated at the preliminary motion estimate $\bar{\mathbf{u}}$, are used as input for our confidence network and for training the data term via a maximum likelihood criterion (c.f. Sec. 2.6).

2.2 Quad-Fitting

Our procedure above limits our candidate flow to take only even integral values, due to the sampling and additional striding imposed on the feature maps. While the striding increases the admissible motion magnitude of our cost volume, the local (sub-)pixel accuracy suffers. Our solution is to refine the location by fitting a quadratic at the predicted motion and return its arg min and cost. To that end, we up-sample and scale the preliminary motion estimates $\bar{\mathbf{u}}$ and fit the quadratic in the vicinity of the initial match. Using nearest neighbor interpolation we can – at each non-boundary pixel – identify 4 motion candidates in the up-sampled motion field that are investigated for a refinement. Here, we fit a quadratic at the position (of the 4 candidates) of minimal cost and update the displacement to sub-pixel accuracy by solving the quadratic equation. To fit the quadratic, we utilize the high-resolution feature maps ψ , acquired before the striding in the feature generation takes place. We use a 5 stencil around the predicted match that is given by $(\bar{v}_0, \bar{v}_1) := \arg \min_{v_0 \in \{2\bar{u}_0, 2\bar{u}_0+1\}, v_1 \in \{2\bar{u}_1, 2\bar{u}_1+1\}} -\langle \psi^0(x, y), \psi^1(x+v_0, y+v_1) \rangle$. We fit a quadratic function $f(\mathbf{v}) := \sum_i a_i v_i^2 + b_i v_i + c$ to the (negative) correlation $q_{x,y,v_0,v_1} := -\langle \psi^0(x, y), \psi^1(x + \bar{v}_0 + v_0, y + \bar{v}_1 + v_1) \rangle$ between the respective feature vectors in both images. Abbreviating the negative correlation cost with q_{x,y,v_0,v_1} the solution to the fitting problem becomes:

$$a_0 = \frac{q_{x,y,+1,0} + q_{x,y,-1,0} - 2q_{x,y,0,0}}{2}, \quad b_0 = \frac{q_{x,y,+1,0} - q_{x,y,-1,0}}{2}, \quad c = q_{x,y,0,0} \quad (5)$$

$$a_1 = \frac{q_{x,y,0,1} + q_{x,y,0,-1} - 2q_{x,y,0,0}}{2}, \quad b_1 = \frac{q_{x,y,0,1} - q_{x,y,0,-1}}{2} \quad \text{and solution} \quad (6)$$

$$v_0 = \frac{-b_0}{2a_0}, \quad v_1 = \frac{-b_1}{2a_1} \quad \text{with } f(v_0, v_1) = a_0 v_0^2 + b_0 v_0 + c + a_1 v_1^2 + b_1 v_1. \quad (7)$$

If the fitting fails, the motion estimate $\bar{\mathbf{v}}$ is not a local minimum of the cost w.r.t. ψ and we return the integral flow $\bar{\mathbf{v}}$ and cost at that pixel. Otherwise we set $\hat{\mathbf{u}} := \bar{\mathbf{v}} + \mathbf{v}$. The second row of Fig. 2 shows a typical result for $\hat{\mathbf{u}}$ of our fitting layer. Subpixel accuracy can only be achieved if the initial discrete flow $\bar{\mathbf{u}}$ returned as the arg min solution of the correlation volume is close to the ground-truth. We embed our fitting procedure into a single network layer.

Backpropagation only requires us to compute the derivatives of the expression above w.r.t. the feature vectors ψ . Empirically, compared to directly matching features at the finest resolution, our combination of striding and quad-fitting leads to a smaller sized correlation volume and sub-pixel accuracy.

2.3 Diffusion Tensor

To compute the diffusion tensor, we apply a simple 4 layer feed-forward network with 64 channels and relu non-linearities between 3×3 convolutions with dilations of size 1, 2 and 4 on the input image I^0 . By using dilations we operate at the finest resolution, but aggregate information of a larger spatial context [39]. To obtain values between 0 and 1 for our 2D tensor W , a final 1×1 convolution is followed by a sigmoid activation function. Fig. 2 (3rd row) shows a typical tensor obtained from an image of the Sintel benchmark. The regularization force is only low near image edges. Otherwise the regularizer of (1) operates at full strength.

2.4 Confidence estimate

Again we prefer a simple network to produce a single confidence estimate per pixel. The input to this stage are the upsampled pseudo-likelihoods (4) of the preliminary motion estimates $\bar{\mathbf{u}}$, the upsampled distances between forward and backward flow vectors, $d(\bar{\mathbf{u}}, \bar{\mathbf{u}}^{\text{BW}})$, the distance to the boundary of the warped pixels, $b(\hat{\mathbf{u}})$, and the costs after the quadratic fit (7). The forward-backward distance is computed by linear interpolation of the backward flow vectors, i.e. $d(\bar{\mathbf{u}}, \bar{\mathbf{u}}^{\text{BW}}) := |\bar{\mathbf{u}}(x, y) - \bar{\mathbf{u}}^{\text{BW}}(x + \hat{u}_0, y + \hat{u}_1)|$. Assuming images of $N \times M$ pixels the distance to the boundary is given by $b(\hat{\mathbf{u}}) := \max(0, \min(x + \hat{u}_0, y + \hat{u}_1, N - x - \hat{u}_0, M - y - \hat{u}_1))$. We further apply non-minimum suppression on the high resolution confidence map. Of the four pixels covered by one pixel of the low dimensional feature map, we only allow $c > 0$ for the one of maximum confidence.

We posit, that all inputs to the network contribute some independent information that can be exploited for our confidence score: a forward-backward check can identify occlusions and demand consistency, the arg min flow can lead to higher confidence in smooth regions than in noisy ones, a criterion also investigated in e.g. [16]. By design, the softmax-probabilities are directly related to the confidence, whereas the fitting score can provide similar information, but in a more local vicinity. The network architecture is again given by a sequence of dilated 3×3 convolutions with relu activations, followed by a single 1×1 convolution with a sigmoid activation function. We employ seven layers with empirically chosen dilations of size 1, 2, 4, 8, 4, 2 and 1 for the final 1×1 convolution that produces the 1D confidence signal. Fig. 2 (2nd row, right) visualizes the confidence scores for the example. We observe that confident pixels are rare, and that those occur mostly close, but in some distance to the edges in the image.

2.5 Optimization Layer

Given the input from the stages above we can compute the solution to (1) or (2) by unrolling iterations of a first-order algorithm. The non-smooth convex

problem has a composite (smooth plus non-smooth) structure that allows the application of FISTA [4], which has optimal convergence rate $\frac{1}{k^2}$ after k iterations [24]. Yet, the very sparse data term (c.f. Fig. 2), leads to a situation that requires many iterations to achieve convergence for our diffusion like algorithm with local updates. A naive implementation in a high-level language like Tensorflow or Theano [34], would demand $O(KNM)$ memory to perform backpropagation over K iterations and NM pixels, which is too much to handle for current GPU hardware. Likewise, accumulating gradients over many iterations in single precision can be numerically troublesome. Here, we show that it can be beneficial to implement the optimization stage of such first order algorithms, including backpropagation, within in a single layer in order to reduce memory overhead and make end-to-end training feasible. To that end, we combine two simple ideas, the gradient checkpointing technique [14] and accumulating the gradients into a buffer of double precision, such that the core of our algorithm can still run in the much more efficient single precision on the GPU. Checkpointing reduces the memory requirements to $O(\sqrt{K}NM)$ at the cost of a second forward pass. At $K \sim 10^4$ this leads to savings of a factor of 100 and, hence, we can backpropagate gradients over 10000 iterations without numerical problems. In practice, we introduce $O(\sqrt{K})$ checkpoints every $\lceil k\sqrt{K} \rceil, k = 0 \dots \lfloor \sqrt{K} \rfloor$ iterations at which we store the necessary information to reproduce a forward pass from $\lceil k\sqrt{K} \rceil$ to iteration $\lceil (k+1)\sqrt{K} \rceil$. This procedure demands $O(\sqrt{K}NM)$ storage. To perform backpropagation, we go backwards from checkpoint to checkpoint and recover the information needed to perform backpropagation between two checkpoints with a second forward pass. Again, this requires $O(\sqrt{K}NM)$ intermediate memory, which can be released afterwards. We then compute the gradients of this stage and, at the end, accumulate them into buffers of double precision.

We focus our analysis on the TV like inpainting functional (1). After discretization on a cartesian grid of size $N \times M$, the problem to determine $u_i \in \mathbb{R}^{NM}$, the pixelwise flow in each coordinate direction $i = 0, 1$ can be written as

$$\min_{u_i} \|\sqrt{W}Du_i\|_\delta + \|u_i - \hat{u}_i\|_c. \quad (8)$$

The linear mapping $D: \mathbb{R}^{NM} \rightarrow \mathbb{R}^{2NM}$ approximates the spatial gradient of the flow per direction via finite forward differences and $W: \mathbb{R}^{2NM} \rightarrow \mathbb{R}^{2NM}$ represents the discretized diffusion tensor and accordingly weighs the contribution of each local gradient per direction. The Huber norm $\|\cdot\|_\delta$ operates on each local gradient individually. The norm $\|\cdot\|_c$ denotes the ℓ_1 norm weighted by the confidence c . Our optimization procedure can be described by the following FISTA step:

$$u_i^{k+0.5} := v_i^k - D^\top \frac{W}{\max(1, |\sqrt{W}Dv_i^k|_2/\delta)} Dv_i^k \quad (9)$$

$$u_i^{k+1} := \begin{cases} u_i^{k+0.5} - c & \text{if } u_i^{k+0.5} - c > \hat{u}_i \\ u_i^{k+0.5} + c & \text{if } u_i^{k+0.5} + c < \hat{u}_i \\ \hat{u}_i & \text{else} \end{cases} \quad (10)$$

$$v_i^{k+1} := u_i^{k+1} + \frac{t^k - 1}{t^{k+1}} (u_i^{k+1} - u_i^k), \quad (11)$$

which is executed for $i=0,1$ in parallel and K iterations. The solution returned, u_i^K , is one of the components of \mathbf{u} , and $t^k \in \mathbb{R}$ denote the step-sizes. In contrast to [35] we leave learning the step-sizes for future work and use $t^k := \frac{1+\sqrt{1+4t^{k-1}}}{2}$ for $k > 0$ and $t^0 := 1$, as advocated in the original FISTA paper. This scheme guarantees a $\frac{1}{k^2}$ convergence rate [4]. We can incorporate the Lipschitz constant L into our Tensor $W := 1/L \cdot W$. Later, the gradients $\frac{\partial f}{\partial W}$ w.r.t. W have to be adjusted accordingly, we simply return $L \frac{\partial f}{\partial W}$. Here, L is the maximal eigenvalue of our system matrix $D^\top W D$, e.g. for TV we have $L = 8$. Given the gradient of some loss function f on our returned solution u^K from the forward pass, $\frac{\partial f}{\partial u^K}$, we have to compute the gradients w.r.t. our parameters W , $\hat{\mathbf{u}}$ and c (and β for TGV-inpainting). Our backward algorithm is composed of the following steps and returns $\frac{\partial f}{\partial \hat{u}_i}$, $\frac{\partial f}{\partial c}$, $\frac{\partial f}{\partial W}$ and $\frac{\partial f}{\partial u^0}$, the gradient w.r.t. the initial solution u^0 .

$$\frac{\partial f}{\partial \hat{u}_i} := \frac{\partial f}{\partial \hat{u}_i} + \frac{\partial f}{\partial u_i^{k+1}} \text{ if } c < |\hat{u}_i - u_i^{k+0.5}| \quad (12)$$

$$\frac{\partial f}{\partial c} := \frac{\partial f}{\partial c} + \text{sign}(\hat{u}_i - u_i^{k+0.5}) \frac{\partial f}{\partial u_i^{k+1}} \text{ if } c \geq |\hat{u}_i - u_i^{k+0.5}| \quad (13)$$

$$\frac{\partial f}{\partial u_i^{k+0.5}} := \begin{cases} \frac{\partial f}{\partial u_i^{k+1}} & \text{if } c \geq |\hat{u}_i - u_i^{k+0.5}| \\ 0 & \text{else} \end{cases} \quad (14)$$

$$\frac{\partial f}{\partial v_i^k} := \left(I - \frac{\partial}{\partial v_i^k} \left(\frac{W}{\max(1, |\sqrt{W} D v_i^k|_2 / \delta)} D v_i^k \right)^\top \right) D \frac{\partial f}{\partial u_i^{k+0.5}} \quad (15)$$

$$\frac{\partial f}{\partial W} := \frac{\partial f}{\partial W} + \frac{\partial}{\partial W} \left(\frac{W}{\max(1, |\sqrt{W} D v_i^k|_2 / \delta)} D v_i^k \right)^\top D \frac{\partial f}{\partial u_i^{k+0.5}} \quad (16)$$

$$\frac{\partial f}{\partial u_i^k} := \frac{\partial f}{\partial u_i^k} + \left(1 + \frac{t^{k-1} - 1}{t^k} \right) \frac{\partial f}{\partial v_i^k} \quad (17)$$

$$\frac{\partial f}{\partial u_i^{k-1}} := -\frac{t^{k-1} - 1}{t^k} \frac{\partial f}{\partial v_i^k}. \quad (18)$$

Here, we use the outer products in (15, 16) to achieve a compact notation. In our implementation, we exploit the extreme sparsity of the resulting matrix.

Most of the above lines are a direct application of the chain rule, however, we briefly show how to arrive at (16). Looking at a single gradient of index l , $\frac{\partial f}{\partial W_l}$, the chain rule suggests that $\frac{\partial f}{\partial W_l} = \sum_k \left(\frac{\partial f}{\partial u_i^{k+0.5}} \right)^\top \frac{\partial u_i^{k+0.5}}{\partial W_l}$ and $\frac{\partial u_i^{k+0.5}}{\partial W_l} = D^\top \left(\frac{\partial}{\partial W_l} \frac{W}{\max(1, |\sqrt{W} D v_i^k|_2 / \delta)} \right) D v_i^k$. While this justifies our summation over the iterations, we also observe that $\frac{\partial}{\partial W_l} \left(\frac{W}{\max(1, |\sqrt{W} D v_i^k|_2 / \delta)} \right)$ is the zero matrix except at indices l and $l+1$, where we assume wlog. that $l+1$ indicates the co-dimension of the diffusion tensor at the pixel. If we let W_l^{l+1} denote the 2×2 submatrix at row and column indices $l, l+1$ of the diagonal matrix $\frac{W}{\max(1, |\sqrt{W} D v_i^k|_2 / \delta)}$, we

find $\frac{\partial f}{\partial W_l} = \left(D \frac{\partial f}{\partial u_i^{k+0.5}} \right)_l^{l+1} \left(\frac{\partial}{\partial W_l} W_l^{l+1} \right) (D v_i^k)_l^{l+1}$, which equals $\frac{\partial f}{\partial W}$ of (16) at the respective index l . Finally, note that the matrix in (15) also has non-zero entries for – in backward direction – horizontal and vertical neighbors of a pixel.

Algorithmically backpropagation works as follows. Our checkpoint variables are u_i^k and v_i^k from which we recover all $u_i^{k+0.5}$ and v_i^k for a whole stage. Given $\frac{\partial f}{\partial u^k}$, we once apply (12-14) to initialize $\frac{\partial f}{\partial u^{k-0.5}}$ along with $\frac{\partial f}{\partial \hat{u}_i}$ and $\frac{\partial f}{\partial c}$. Per iteration k we already know $\frac{\partial f}{\partial u^{k+0.5}}$, $u_i^{k-0.5}$ and v_i^k and can execute Eqs. 15–18 followed by Eqs. 12–14 for iteration number $k-1$ to recover $\frac{\partial f}{\partial u^{k-0.5}}$ and we can continue with the next iteration by repeating these steps. Because $\frac{\partial f}{\partial u_i^{k-1}}$ from (18) is required in (17) the values have to be kept in memory for one iteration.

The TGV case (2) is slightly more involved, but the derivations are similar. Discretization leads to the objective:

$$\min_{u_i} \min_{w_i=(w_{i,0}, w_{i,1})^\top} \|\sqrt{W}(Du_i - w_i)\|_\delta + \beta(\|Dw_{i,0}\|_\delta + \|Dw_{i,1}\|_\delta) + \|u_i - \hat{u}_i\|_c, \quad (19)$$

with auxiliary variables $w_{i,j} \in \mathbb{R}^{NM}$, $i, j \in \{0, 1\}$. We define the operator $B : \mathbb{R}^{3NM} \rightarrow \mathbb{R}^{6NM}$ by stacking the linear operations in (19) into a single mapping and likewise define the matrices $V_\beta : \mathbb{R}^{6NM} \rightarrow \mathbb{R}^{6NM}$ and $V : \mathbb{R}^{6NM} \rightarrow \mathbb{R}^{6NM}$. With I denoting the identity mapping, $I : \mathbb{R}^{4NM} \rightarrow \mathbb{R}^{4NM}$, we define V_β by stacking the W and βI into a single diagonal matrix. To construct V we omit the multiplication of the unit matrix I with β . As before, the Lipschitz constant $L = \max(12, 8\beta)$ is incorporated into the operators V_β and V and the respective gradient $\frac{\partial f}{\partial V_\beta}$ is adjusted; again we return $L \frac{\partial f}{\partial V_\beta}$. Then the forward path becomes:

$$(u_i^{k+0.5}, w_i^{k+1})^\top := (v_i^k, q_i^k)^\top - B^\top \frac{V_\beta}{\max(1, |\sqrt{V} B (v_i^k, q_i^k)^\top|_2 / \delta)} B (v_i^k, q_i^k)^\top \quad (20)$$

$$u_i^{k+1} := \begin{cases} u_i^{k+0.5} - c & \text{if } u_i^{k+0.5} - c > \hat{u}_i \\ u_i^{k+0.5} + c & \text{if } u_i^{k+0.5} + c < \hat{u}_i \\ \hat{u}_i & \text{else} \end{cases} \quad (21)$$

$$(v_i^{k+1}, q_i^{k+1})^\top := (u_i^{k+1}, w_i^{k+1})^\top + \frac{t^k - 1}{t^{k+1}} (u_i^{k+1}, w_i^{k+1})^\top - (u_i^k, w_i^k)^\top, \quad (22)$$

The complete backward path for TGV inpainting is presented in the supplementary material. Algorithmically we operate in the same manner as described for the TV case. In both cases we set δ to 0.1. Please note that instead of learning a single scalar β , the algorithm can be extended to learn a pixel-wise diffusion tensor that operates on the auxiliary variables w_0, w_1 in (19).

Hierarchical Optimization. Although we do not experience problems when training our network for 10K iterations at full resolution, a simple hierarchical strategy proves to be more efficient. At first we solve (8) at a lower resolution, using down-sampled versions of c , W and \hat{u} to initialize u^0 . At the next level c , W and \hat{u} are set accordingly, but u^0 is initialized by up-sampling the solution of the coarser level. Requiring fewer iterations at the finest level, this strategy accelerates the optimization. Here, we use 3 levels with 2K, 2K and 4K iterations.

2.6 Training

We start with the feature generation and pretrain this part of the network. Apart from the log-likelihood term (4), our loss function also considers the quad-fitting procedure. Given the ground-truth flow \mathbf{u}^* , we define the loss function

$$L_{\text{cor}}(\hat{u}_0, \hat{u}_1) := \sum_{(x,y) \in \Omega} \log p_0(x, y, u_0^*) + \log p_1(x, y, u_1^*) + \alpha \min(1, |\hat{\mathbf{u}} - \mathbf{u}^*|_\epsilon), \quad (23)$$

where we use $\epsilon = 0.01$ for the Huber-norm and define the lookup by rounding the continuous \mathbf{u}^* and set $\alpha = 0.1$. Further, we use the up-sampled softmax probabilities in (23) and take care to not pass the gradients implied by the quad-fit through to the argmin lookup and correlation volume. Equipped with a trained and, in this work from now, fixed feature generation part, we further train the rest of the network by measuring the Huber-norm w.r.t. the ground truth. We set our displacement range to $d = 96$ in each direction and note that it is effectively doubled, due to our striding/quad-fitting methodology. All our trainings are run on full images without down-sampling or cropping the input.

3 Evaluation

We train our networks with the Theano package [34] on a machine equipped with a NVIDIA Titan X GPU with 12 GB of RAM. Our training data consists of either the artificial Sintel data set [7] or both of the KITTI [13,22] data sets. KITTI targets an automotive setting and provides real world scenes, but only sparse and approximately correct ground truth. When training on Sintel we use 441 of the 1041 images for training and use the other images for validation and evaluation. The KITTI data is divided in a similar manner. An implementation of our custom layers (quad-fitting, TV/TGV inpainting) can be found online ¹.

Memory and Runtime. Overall our network has 450K parameters. Training the feature generation on full sized Sintel images requires 4GB, the same amount is used for training the full inpainting network with backpropagation disabled for the pretrained part. In both cases, most of the memory is used by the correlation volumes, despite min-projection and down-sampling. A full joint training is left for future work. Our optimization layer proves to be a lightweight contribution to the network, requiring only additional 600MB of GPU memory at training time. A forward pass of the network requires 0.4s on a full sized image.

3.1 Qualitative Evaluation

We show a few results in Fig. 3 for the TV based inpainting on Sintel and in Fig. 4 for our TGV model on KITTI. The hard Sintel examples lead to a noisy arg min solution (4th row) and confident pixels (2nd row) are rare. The network appears to prefer only few correct matches, which in turn demands many iteration to

¹ <https://github.com/vogechri/CustomNetworkLayers>

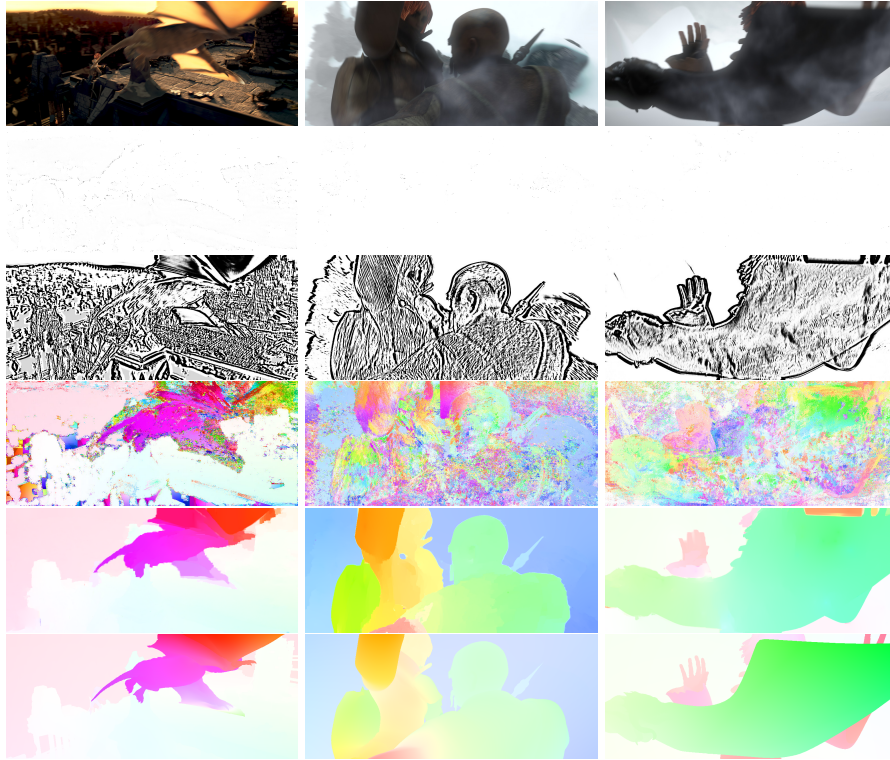


Fig. 3. Example results from the Sintel training data set [7]. From top to bottom: input image I^0 , confidence c , horizontal component of the diffusion tensor W , arg min solution, solution after the optimization layer and the ground truth.

spread the information. For the simpler left example the confident pixels outline the image and arg min-flow edges (zoom in). Interestingly, compressive inpainting models [8] also prefer those kind supporting matches for their diffusion process. Those appear to possess the highest information content. The KITTI examples possess less sharp edges than the results on Sintel. We suspect the sparse ground truth, lacking information at object edges, to cause this phenomenon.

3.2 Quantitative Evaluation

We start with the results for the Sintel data set in Tab. 1. The TV-model can improve the 'matching only' solution after quad fitting by a significant amount. TGV performs about 10% worse than TV. Note that for TGV more correct matches (3) are required to inpaint an affine motion in a segmented region than for TV (only 1). Training a TV-model with 10 times less iterations leads to significantly worse results. We observe that the higher the number of iterations, the sparser the confidence can be chosen; in other words, the stricter the selection

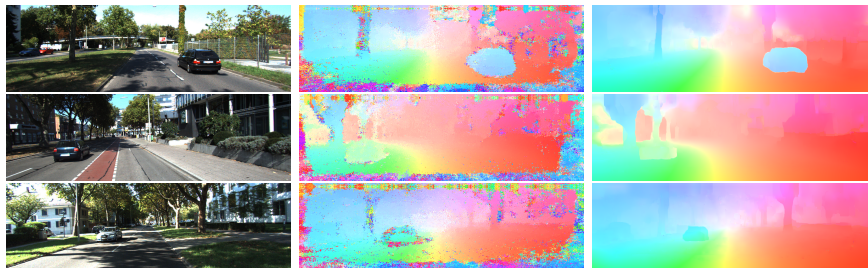


Fig. 4. *Left:* Example from the KITTI training set [22]. *Middle:* The arg min solution, \hat{u} , used as input to the optimization layer. *Right:* Our inpainted solution (TGCV variant).

Table 1. Results on the Sintel training set (final). Displayed are end-point error (EPE) and percentage of outliers (Out), deviating > 3 pixels from the ground truth for unoccluded (Noc) and all pixels (Occ). Investigated methods include *Quad-fit*: Results after the quadratic fit, *TV-Model*: TV inpainting (1), *TGCV-Model*: TGCV inpainting (2), $n \times TV$ -Model: TV inpainting trained using n times the default number of iterations in (9-11), L_2^2 -Reg: quadratic regularizer, L_2^2 -All: quadratic on confidence and regularizer.

Model	EPE (Noc)	> 3 px. (Noc)	EPE (Occ)	> 3 px. (Occ)
Quad-fit	11.27	17.16%	–	–
TV-Model	1.64	7.63%	2.48	10.29 %
TGCV-Model	1.81	7.79%	2.68	10.42 %
$0.1 \times TV$ -Model	3.11	10.01%	5.69	13.79 %
L_2^2 -Reg.(TV)	2.21	8.38%	3.02	11.06 %
L_2^2 -All (TV)	2.56	9.29%	3.70	12.23 %

Table 2. Results on the Kitti training set. Investigated methods include. *TGCV-Model*: TGCV inpainting (2). *bi-Laplacian*: Inpainting based bi-Laplacian described in the text.

Model	Noc				Occ			
	EPE	3px.	4px.	5px.	EPE	3px.	4px.	5px.
TGCV-Model	1.73	8.16%	6.33%	5.26 %	3.36	12.83%	10.52%	9.06 %
TV-Model	1.85	9.90%	7.71%	6.36 %	6.93	23.53%	19.43%	16.53 %
bi-Laplacian	2.19	10.42%	8.07%	6.53 %	4.17	15.70%	12.97%	11.38 %

becomes. Finally, we also investigate if it is worthwhile to use a robust, non-smooth energy model or whether a linear model, as used in, e.g., [3] already suffices. In the fifth row we replace the Huber norm in (1) with a quadratic term. In the last row we introduce the square also on the ℓ_1 term in (1). The results gradually worsen the smoother the energy becomes. The complete linear model delivers results that are about 50% worse. The network seems unable to compensate the lost robustness via diffusion tensor and confidence map alone.

On KITTI (Tab. 2) the TV based model cannot compete with the robust TGCV model (2) with a well studied bi-Laplacian model: $\arg \min_{u_i} \int_{\Omega} |W^{\frac{1}{2}} \Delta u_i|_2^2 + c|u_i - \hat{u}_i|_2^2 dx$,

Table 3. Results on the Sintel [7] (final) and KITTI [22] test sets. Displayed are endpoint error (EPE) for Sintel and percentage of outliers for KITTI. Investigated methods include our submissions (*TV*) and (*TGV*) and related methods from the benchmark.

	(TV)	(TGV)	[17]	[41]	[28]	[15]	[20]	[33]	[27]
[7] EPE (Noc)	2.70	-	2.77	2.79	3.06	2.62	2.4	2.4	4.5
[7] EPE (Occ)	6.12	-	5.62	6.04	6.29	5.73	5.4	5.0	8.4
[22] % > 3px. (Noc)	-	10.8	10.3	13.6	16.7	12.4	5.5	5.1	26.7
[22] % > 3px. (Occ)	-	15.6	18.8	22.8	26.3	21.2	9.4	7.9	35.1

$i = 0, 1$, where Δ is the Laplacian matrix. Again the linear model performs worse than our robust model, trailing its results by about 20%.

Tab. 3 compares our submitted models with a selection of inpainting based competitors on the official test set of both benchmarks. At first we notice a significant performance drop for both benchmarks, compared to the training set. On KITTI our network outperforms all three inpainting models Epic-Flow [28], [17] and the inpainting network of [41] by a large amount, although all either employ an affine model [28,17] or can learn one [41]. Our method even outperforms [15], who process the cost volume with a MRF model, before using [28] for inpainting. On Sintel our model performs on par or better than competing methods, but only for non occluded regions. Measuring all pixels our method trails [17] and [15]. However, recall that [17] starts from a much better initial flow [19] that is already on par with our approach in this metric. In fact many methods on the benchmark are not stand-alone, but utilize some well performing model for initialization or employ multiple post-processing steps. Here, our optimization layer could serve as a differentiable inpainting algorithm within a larger network.

Our model trails the current state-of-the-art [33,20] as shown Tab. 3. Yet, we use 10 ([20]) or 17 ([33]) times less parameters. Even [27] uses more than twice the number of parameters and clearly performs worse. Further, our model is minimalistic by design, employs no post-processing and can be used as complementary step for other methods, i.e. by replacing our initial flow $\hat{\mathbf{u}}$ with theirs.

4 Conclusion

We proposed a simple model for the accurate inpainting of optical flow, using an interpretable network to deliver the inputs for an optimization stage. In the course of this work we proposed two non-custom layers, one for subpixel-refinement and one for optimization of our inpainting energy. For the latter, we showed that we can run and backpropagate through 10K iterations, which allows to accurately solve our energy problem. While the layer itself could be useful for various tasks, the lessons learned can also be transferred to similar problems.

In the future we would like include 3D cost volume filtering and train the full model end-to-end, including feature generation. Further we believe that learning a selection mechanism for a joint TV/TGV regularization will be of benefit.

References

1. Achanta, R., Shaji, A., Smith, K., Lucchi, A., Fua, P., Susstrunk, S.: Slic superpixels compared to state-of-the-art superpixel methods. *PAMI* (2012)
2. Agresti, G., Minto, L., Marin, G., Zanuttigh, P.: Deep learning for confidence information in stereo and tof data fusion. In: The IEEE International Conference on Computer Vision (ICCV) Workshops (Oct 2017)
3. Barron, J.T., Poole, B.: The fast bilateral solver. *ECCV* (2016)
4. Beck, A., Teboulle, M.: A fast iterative shrinkage-thresholding algorithm for linear inverse problems. *SIAM J. Img. Sci.* (2009)
5. Bredies, K., Kunisch, K., Pock, T.: Total generalized variation. *SIAM J. Imaging Sciences* (2010)
6. Brox, T., Bruhn, A., Papenberg, N., Weickert, J.: High accuracy optical flow estimation based on a theory for warping. In: *ECCV* (2004)
7. Butler, D.J., Wulff, J., Stanley, G.B., Black, M.J.: A naturalistic open source movie for optical flow evaluation. In: A. Fitzgibbon et al. (Eds.) (ed.) *ECCV*. pp. 611–625. Part IV, LNCS 7577, Springer-Verlag (Oct 2012)
8. Chen, T., Xu, B., Zhang, C., Guestrin, C.: Training deep nets with sublinear memory cost. *CoRR* [abs/1604.06174](https://arxiv.org/abs/1604.06174) (2016)
9. Chen, Y., Ranftl, R., Pock, T.: A bi-level view of inpainting - based image compression. *CoRR* [abs/1401.4112](https://arxiv.org/abs/1401.4112) (2014)
10. Dollár, P., Zitnick, C.L.: Structured forests for fast edge detection. In: *CVPR*. pp. 1841–1848. *ICCV '13, IEEE* (2013)
11. Dosovitskiy, A., Fischer, P., Ilg, E., Häusser, P., Hazırbaş, C., Golkov, V., v.d. Smagt, P., Cremers, D., Brox, T.: FlowNet: Learning optical flow with convolutional networks. In: *ICCV* (2015)
12. Galić, I., Weickert, J., Welk, M., Bruhn, A., Belyaev, A., Seidel, H.P.: Image compression with anisotropic diffusion. *Journal of Mathematical Imaging and Vision* **31**(2), 255–269 (Jul 2008). <https://doi.org/10.1007/s10851-008-0087-0>
13. Geiger, A., Lenz, P., Urtasun, R.: Are we ready for autonomous driving? In: *CVPR* (2012)
14. Griewank, A., Walther, A.: Algorithm 799: Revolve: An implementation of checkpointing for the reverse or adjoint mode of computational differentiation. *ACM Trans. Math. Softw.* **26**(1), 19–45 (Mar 2000)
15. Güney, F., Geiger, A.: Deep discrete flow. In: *Asian Conference on Computer Vision (ACCV)* (2016)
16. Hu, X., Mordohai, P.: A quantitative evaluation of confidence measures for stereo vision. *IEEE Trans. Pattern Anal. Mach. Intell.* **34**(11), 2121–2133 (Nov 2012)
17. Hu, Y., Li, Y., Song, R.: Robust interpolation of correspondences for large displacement optical flow. In: *CVPR*. *IEEE* (2017)
18. Hu, Y., Song, R., Li, Y.: Efficient coarse-to-fine patchmatch for large displacement optical flow. In: *The IEEE Conference on Computer Vision and Pattern Recognition (CVPR)* (June 2016)
19. Hu, Y., Song, R., Li, Y.: Efficient coarse-to-fine patchmatch for large displacement optical flow. In: *CVPR*. *IEEE* (2016)
20. Hui, T.W., Tang, X., Change Loy, C.: Liteflownet: A lightweight convolutional neural network for optical flow estimation. In: *CVPR* (2018)
21. Ilg, E., Mayer, N., Saikia, T., Keuper, M., Dosovitskiy, A., Brox, T.: FlowNet 2.0: Evolution of optical flow estimation with deep networks. In: *CVPR* (2017)
22. Menze, M., Geiger, A.: Object scene flow for autonomous vehicles. In: *CVPR* (2015)

23. Munda, G., Shekhovtsov, A., Knöbelreiter, P., Pock, T.: Scalable full flow with learned binary descriptors. In: GCPR. pp. 321–332 (2017)
24. Nesterov, Y.: A method of solving a convex programming problem with convergence rate $O(\frac{1}{k^2})$. Soviet Mathematics Doklady (1983)
25. Peter, P., Hoffmann, S., Nedwed, F., Hoeltgen, L., Weickert, J.: From optimised inpainting with linear pdes towards competitive image compression codecs. In: PSIVT. pp. 63–74. Springer-Verlag New York, Inc. (2016)
26. Poggi, M., Tosi, F., Mattoccia, S.: Quantitative evaluation of confidence measures in a machine learning world. In: ICCV (Oct 2017)
27. Ranjan, A., Black, M.J.: Optical flow estimation using a spatial pyramid network. In: CVPR (2017)
28. Revaud, J., Weinzaepfel, P., Harchaoui, Z., Schmid, C.: Epicflow: Edge-preserving interpolation of correspondences for optical flow. In: CVPR. IEEE (2015)
29. Rhemann, C., Hosni, A., Bleyer, M., Rother, C., Gelautz, M.: Fast cost-volume filtering for visual correspondence and beyond. In: CVPR. pp. 3017–3024. IEEE (2011)
30. Riegler, G., Rüther, M., Horst, B.: Atgv-net: Accurate depth super-resolution. In: European Conference on Computer Vision (2016)
31. Rudin, L.I., Osher, S., Fatemi, E.: Nonlinear total variation based noise removal algorithms. Phys. D (1992)
32. Sun, D., Yang, X., Liu, M.Y., Kautz, J.: Pwc-net: Cnns for optical flow using pyramid, warping, and cost volume. In: CVPR (2018)
33. Sun, D., Yang, X., Liu, M.Y., Kautz, J.: Pwc-net: Cnns for optical flow using pyramid, warping, and cost volume. In: CVPR (2018)
34. Theano Development Team: Theano: A Python framework for fast computation of mathematical expressions. CoRR (2016)
35. Vogel, C., Pock, T.: A primal dual network for low-level vision problems. In: Pattern Recognition - 39th German Conference, GCPR 2017, Basel, Switzerland, September 12-15, 2017, Proceedings. pp. 189–202 (2017)
36. Wang, S., Fanello, S.R., Rhemann, C., Izadi, S., Kohli, P.: The global patch collider. In: CVPR. IEEE (July 2016)
37. Weinzaepfel, P., Revaud, J., Harchaoui, Z., Schmid, C.: DeepFlow: Large displacement optical flow with deep matching. In: ICCV. IEEE, Sydney, Australia (Dec 2013)
38. Werlberger, M., Trobin, W., Pock, T., Wedel, A., Cremers, D., Bischof, H.: Anisotropic Huber-L1 optical flow. In: BMVC (2009)
39. Yu, F., Koltun, V.: Multi-scale context aggregation by dilated convolutions. In: ICLR (2016)
40. Zheng, S., Jayasumana, S., Romera-Paredes, B., Vineet, V., Su, Z., Du, D., Huang, C., Torr, P.: Conditional random fields as recurrent neural networks. In: ICCV (2015)
41. Zweig, S., Wolf, L.: Interponet, a brain inspired neural network for optical flow dense interpolation. In: CVPR. pp. 6363–6372 (2017)